crystals

MDPI

Article

Effect of Changing and Combining Trivalent Metals in the Structural and Electronic Properties of Cu-Based Crystal Delafossite Materials

Joeluis Cerutti Torres [1,2,*], Pablo Sánchez-Palencia [2], José Carlos Jiménez-Sáez [1], Perla Wahnón [2] and Pablo Palacios [1,2,*]

[1] Departamento de Física Aplicada a las Ingenierías Aeronáutica y Naval, ETSI Aeronáutica y del Espacio, Universidad Politécnica de Madrid, Pz. Cardenal Cisneros, 3, 28040 Madrid, Spain; jc.jimenez@upm.es
[2] Instituto de Energía Solar, ETSI Telecomunicación, Universidad Politécnica de Madrid, Ciudad Universitaria, s/n, 28040 Madrid, Spain; pablos-p94@hotmail.com (P.S.-P.); perla.wahnon@upm.es (P.W.)
* Correspondence: j.ctorres@upm.es (J.C.T.); pablo.palacios@upm.es (P.P.)

Abstract: Cu-based ternary oxides with delafossite structure have received considerable attention in recent years for their versatility in a wide range of applications, among which is the possibility to use them in heterostructure solar cells as hole transport layers, due to their promising behavior as p-type conducting oxides. Ab initio calculations have been performed with density functional theory to investigate the role of the trivalent metal within the $CuMO_2$ structure and the dependence of structural and electronic properties with the species (M = Al, Ga, In, Fe, Cr, Co, Sc, Y) occupying the site of the metal. Generalized Gradient Approximation also including a Hubbard term and nonlocal Heyd–Scuseria–Enzerhof screened hybrid functional schemes were tested and their results were compared. Excellent agreement with experimental lattice parameters and measured gaps have been found. The use of hybrid functionals in HSE approximation considerably improves the bandgaps when compared with the experimental results but takes considerable time to converge, hence the need to explore less demanding methodologies. Trends in the geometry as well as in the electronic properties are discussed, and the effect of mixing different metals ($CuM_xN_{1-x}O_2$, M, N being the aforementioned elements) in the geometry and electronic properties of these delafossite materials is investigated. Due to the high cost of HSE calculations, especially when supercells are needed to model several x concentrations, statistical models and techniques based on machine learning have also been explored to predict HSE bandgap values from GGA and structural information.

Keywords: delafossites; DFT; machine learning

Citation: Cerutti Torres, J.; Sánchez-Palencia, P.; Jiménez-Sáez, J.C.; Wahnón, P.; Palacios, P. Effect of Changing and Combining Trivalent Metals in the Structural and Electronic Properties of Cu-Based Crystal Delafossite Materials. *Crystals* **2024**, *14*, 418. https://doi.org/10.3390/cryst14050418

Academic Editor: Thomas M. Klapötke

Received: 20 March 2024
Revised: 19 April 2024
Accepted: 28 April 2024
Published: 29 April 2024

1. Introduction

The discovery of p-type transparent conductivity of $CuAlO_2$ films with delafossite structure [1] was a milestone in the race for finding p-type transparent conducting oxides (TCOs). These kinds of materials, among which electronic doped ZnO and SnO_2 are perhaps the most representative [2–5], have some very unusual physical properties; they are transparent, similar to glass, but conductive almost like a metal. They are widely used in a variety of electronic applications, from panel displays and touch screens to solar cell applications. In the design of heterostructure solar cells, they are mainly used as electron (ETL) and hole (HTL) transport layers. Problems arise with the fact that most TCOs are n-type conductors, and finding p-type conductors with wide bandgap and good conductivity has been elusive.

It has been discussed [3,4,6] that for semiconductor oxides, the mobility of doping holes at the top of the valence band, typically filled by O-2p bands, tends to be very low due to the strong localization of these levels. Possible solutions to achieve higher mobility of holes would be the use of materials for which the valence band edge is not O-2p but cations

with d electrons at the top of the band or modifying the valence band edge by mixing these orbitals with appropriate cations that have energy-filled levels comparable to those of the O-2p. Allegedly, this would be effective in reducing the strong Coulomb interaction of oxygens and therefore in delocalizing positive holes. The choice of a monovalent copper Cu^{+} as a candidate, with filled $3d^{10}$ orbitals in a closed shell after giving its $4s^{1}$ electron, and energy of the Cu-3d levels compared to those of the O-2p leads to the idea of Cu oxides as good candidates to overcome the localization of holes via covalent bonding between the Cu^{+} and the O^{-2} ions. However, the simplest Cu oxide, CuO_2, has a rather small bandgap and it is not transparent in visible light, despite not having a considerably large conductivity.

Therefore, the discovery of p-type conductivity in $CuAlO_2$ triggered an increased interest in the experimental and theoretical characterization of this compound [3,7–9]. $CuAlO_2$ was followed by the family of $CuM^{III-A}O_2$ metals, in which the M^{III-A} cation is a metal from the group III-A in the periodic table; $CuGaO_2$ was found to also have p-type conductivity and $CuInO_2$ was found to exhibit the ability to be both n- and p-type doped [2,5,10–15]. Also, $CuScO_2$ [16,17] and $CuYO_2$ [18,19] have been studied, as well as $CuCrO_2$, which has been doped with Mg, exhibiting the highest conductivity but not good transparency [20–24]. To date, numerous Cu ternary oxides with delafossite structure $CuMO_2$ (M = B, Al, Ga, In, Fe, Cr, Sc, Y, etc.), and even some with general formula AMO_2 (where A = Ag, Cu), have been reported with p-type conductivity as high as 10^2 S/cm and high optical transparency (50–85%), depending not only on their chemical compositions but also grain sizes or film deposition methods [4,25–32]. Theoretically, special attention has been received by the Fe-delafossite for the difficulties in its calculation [33–36].

The effect of doping with divalent metals in the delafossite compounds has also been investigated. Other studies of mixed structures are common for different kinds of applications and materials [37,38] and are useful not only to predict properties in novel materials but also for the understanding of underlying mechanisms of the different properties of interest withing given materials. The race to achieve good transparency and conductivity has included the study of Mg-doped delafossites [4,21,22,24,29], Ni- or Ca-doped delafossites [20,39], as well as doping with another trivalent metal in structures with high percentages of substitution [27,40].

In this paper, we aim to study a variety of Cu-based delafossite semiconductors as promising materials for photovoltaic applications in the design of heterostructure solar cells, as hole transport layers (HTLs). We focus on the $CuMO_2$ structure, with M = Al, Ga, In, Co, Sc, Y, Fe, Cr. Geometrical and electronic characterization were performed using the density functional theory for these materials, as described in Section 2: Methodology. The main geometrical characteristics of the two phases in which these delafossites can be found are discussed in Section 3: Structural characterization. A discussion about bandgap values, density of states, and band structure can be found in Section 4: Electronic Structure. Then, the effects in the geometry and bandgap when one of the trivalent metals within the oxides is substituted are tested. Section 5 shows results for $CuM_xN_{1-x}O_2$ structures, with N, M being the same species previously mentioned, and $x = 1/3$. Different relative concentrations for N, M require larger supercells, making the more accurate calculations using hybrid exchange correlation functionals such as HSE prohibitive. Thus, a discussion on statistical models and the use of techniques based on machine learning to describe the correlation between the bandgap values described with the GGA and HSE functionals is presented in Section 6. Finally, some concluding remarks highlighting the fundamental properties of these materials are given.

2. Methodology

Since theoretical simulations have proven to be useful for the understanding of the properties of systems at the atomic level, first-principles calculations were performed to gain an insight into the structural and electronic properties of these Cu-based ternary oxides with delafossite structures.

For this purpose, the atomic positions were optimized and the electronic properties were computed within the density functional theory (DFT) approach, based on the framework of the generalized Kohn–Sham scheme [41,42] in combination with the projector augmented wave (PAW) method [43] for the description of the core electrons and the generalized gradient approximation (GGA) within the Perdew–Burke–Ernzerhof (PBE) formalism [44] for the exchange and correlation term, as implemented in the Vienna ab initio simulation package (VASP) [45–47]. It is well-known that GGA typically underestimates gap values, especially when localized orbitals such as metal *d* or *f* states are present. Hence, for a more accurate electronic description, the Heyd–Scuseria–Ernzerhof hybrid functional with the modified fraction of screened short-range Hartree–Fock exchange (HSE06) [48–50] was also used to calculate the density of states and band energies. Hybrid functional calculation results in a more accurate description of electronic properties for some systems compared to simple DFT calculations with a generalized gradient approximation for the exchange and correlation term in the Kohn–Sham scheme. The higher accuracy, however, is reached at the cost of a higher computational time needed to achieve convergence.

In the search for an alternative method to hold acceptable accuracy with less demanding computational resources, calculations using DFT corrected for on-site Coulomb interactions (DFT + U) [51] were also performed. The inclusion of the so-called Hubbard term (+U) provides an approximate correction for strongly correlated *d* or *f* electrons that are usually inaccurately described with standard GGA functionals. The choice of the U parameter is typically an ad hoc choice, sometimes with empirical information. In the present study, the U value has been chosen such that the valence band description in GGA + U reproduces the shape of the band in the density of state curve obtained with HSE06 calculations, i.e., the value of U for which the position of peaks in the valence band edge is the same as in the HSE simulations. Even when the HSE gap values are not reproduced, having a correctly described valence band allows further calculations with a reasonable computational time cost. Table 1 shows the U values used in this work.

Table 1. Different U values used for the on-site Coulomb interaction scheme (DFT + U).

Element	U (eV)
Cu	6.0
Co	5.2
Cr	5.0
Fe	4.0

To model the tetragonal phase of $CuMO_2$, a unit cell with 12 atoms ($Cu_3M_3O_6$) was used, while for the hexagonal cell, a smaller cell with 8 atoms ($Cu_2M_2O_4$) was needed. To model the $CuM_xN_{1-x}O_2$ mixed structures when $x = 1/3$, the same 12-atom cells were used. However, for the machine learning techniques tested, a small number of calculations were run for which $x = 0.5$ and $x = 1/6$, and for these structures, $1 \times 2 \times 1$ supercells, containing 24 atoms, were built.

The electronic wave functions were expanded in a plane wave basis setup to a kinetic energy cutoff of 450 eV, and the atomic positions were optimized using the conjugate gradient method up until the forces on each atom were less than 0.01 eVÅ^{-1} and the energy convergence less than 10^{-8} eV for the relaxation and GGA calculations, and less than 10^{-5} eV for the calculations with the hybrid functional. The structures with the heaviest atoms—the delafossites, including In and Y—were optimized, including spin–orbit coupling (SOC) [52], but the E_{SOC} falls under 0.1 eV, leading to the conclusion that the effect of spin–orbit coupling does not need to be taken into account with these structures. For the Brillouin zone integration, a $12 \times 12 \times 6$ Monkhorst–Pack scheme k-point mesh was used [53] both for the optimization and electronic structure calculation.

As mentioned before, due to the high cost of running HSE calculations for each of these structures to obtain accurate bandgap values, we also explored the use of statistical

models and more complex techniques based on machine learning to describe the correlation between the bandgap values described with the GGA functional as a first approximation, and those obtained with the HSE functional over already relaxed structures.

The applicability of this approach lies not only in the significant reduction in computational cost when calculating the bandgap values of these materials. It would also allow us to extend the study to new configurations with this delafossite structure which, due to their different relative concentration of elements occupying cationic positions, may require larger supercells for modeling. This would make the cost of HSE calculations practically prohibitive due to the greater number of atoms, but through the implementation of this approach, a simple GGA calculation would be enough to infer a meaningful value of the bandgap for a given configuration.

Several models and combinations of chemical and structural information to describe the compounds have been tested, searching for the best description of the structure–property correlation in this group of materials. In the present manuscript, only the main metrics of the best-performing pair of descriptors (set of features or parameters that better describe the system in an appropriate way for its digestion by the statistical model) and models are shown, together with some remarkable comments, in the corresponding section.

3. Structural Characterization

The delafossite structure of these Cu-based ternary oxides can be appreciated fairly in Figure 1. It shows the atom positions and geometrical structure of the converged unit cell for the $CuAlO_2$ delafossite, as a prototype of the structure. The aforementioned delafossite structure consists of close-packed alternate layers of Cu atoms linearly coordinated with O atoms, forming O-Cu-O dumbbells parallel to the *z* axis, and M-centered octahedra (M = Al, Ga, In, Co, Sc, Y, Cr, Fe) parallel to the *xy* plane. The oxygens on the O-Cu-O dumbbells coordinate to three metal ions each, while metal ions coordinate to eight oxygens, forming the mentioned octahedra. The stacking can occur following an ABCABC pattern, thus forming a trigonal system with a rhombohedral Bravais lattice unit cell with space group $R\bar{3}m$ (symmetry number 166), as shown in Figure 1a, or with an ABAB stacking pattern, thus showing a hexagonal unit cell with $P6_3/mmc$ (no. 194) space group, as shown in Figure 1b.

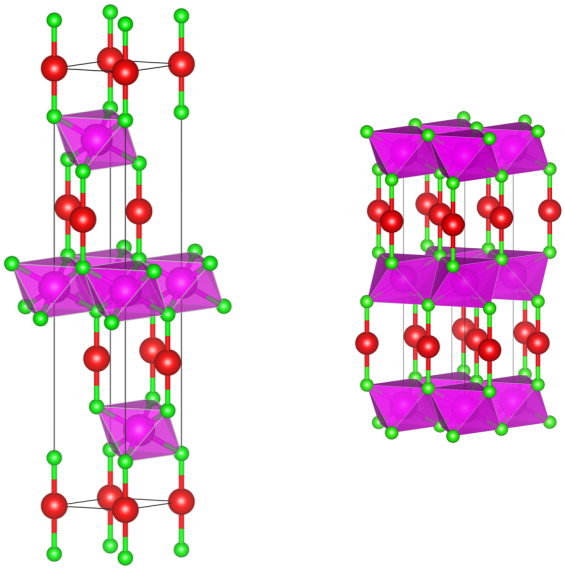

(**a**) 3R phase (**b**) 2H phase

Figure 1. Representation of the delafossite structure in both the (**a**) 3R-rhombohedral and (**b**) 2H-hexagonal phases. Typical delafossite structure in layers can be fairly appreciated. In both cases, Cu atoms are shown in red, O atoms in green, and the transition M atom in magenta spheres.

3.1. Rhombohedral Structures

The structural parameters of the unit cells for the $R\bar{3}m$ phase were calculated and Table 2 summarizes the optimized lattice parameters for all the studied structures, with experimentally measured values for some of the compounds and the deviation percentage that our simulated value represents with respect with the measured one.

Table 2. Lattice parameters *a* and *c* for the studied delafossite in the rhombohedral structure (R3). The relaxed values from our simulations are compared to previous experimental results and the deviation from experimental values is expressed in %. When more than one experimental reference is shown, the deviation written in the Table is the one with the highest absolute value.

	a (Å)		
	Relaxed value	Exp. references	Deviation from exp.
$CuAlO_2$	2.87	2.85 [54], 2.86 [55,56]	+0.7%
$CuGaO_2$	2.97	2.97 [54], 2.98 [55]	−0.3%
$CuInO_2$	3.28	3.29 [57]	−0.3%
$CuCoO_2$	2.86	2.85 [55]	+0.35%
$CuScO_2$	3.19	3.22 [17]	−0.93%
$CuYO_2$	3.47	3.53 [54]	−1.7%
$CuCrO_2$	2.98	2.97 [24], 2.98 [55]	+0.34%
$CuFeO_2$	3.02	3.04 [36,55]	−0.7 %
	c (Å)		
	Relaxed value	Exp. references	Deviation
$CuAlO_2$	17.05	16.94 [55,56], 16.95 [54]	+0.65%
$CuGaO_2$	17.22	17.15 [55], 17.17 [54]	+0.41%
$CuInO_2$	17.62	17.39 [57]	+1.3%
$CuCoO_2$	16.96	16.92 [55]	+0.24%
$CuScO_2$	17.21	17.10 [17]	+0.64%
$CuYO_2$	17.31	17.13 [54]	+1.05%
$CuCrO_2$	17.10	17.09 [24,55]	+0.06%
$CuFeO_2$	17.34	17.17 [36,55]	+0.99%

Our simulations are in good agreement with experimentally measured values for the cells, with deviations that fall under 2% for almost all the compounds, except for the $CuYO_2$, which exhibits the highest deviation for both *a* and *c* parameters. Particularly good agreement between experimental values and our simulations was obtained for *Ga*-, *Co*-, and *Cr*- delafossites.

The role of the trivalent metal ion in the structural and electronic properties of these materials has been discussed [16,19,28,58]. The Cu-Cu distance (equal to the *a* lattice constant, since Cu atoms are in the corners of the unit cell) has been pointed out as playing a relevant role for p-type mobility [58] with holes hopping between Cu ions. On the other hand, the size of the metal ion seems decisive for the *a* constant. Note, in Table 2, the trends followed by the *a* constant for $CuAlO_2$, $CuGaO_2$, $CuInO_2$, $CuScO_2$, and $CuYO_2$, for example. It is strictly true for $CuAlO_2$, $CuGaO_2$, and $CuInO_2$, as well as for $CuScO_2$ and $CuYO_2$ in separate groups. Put together, with $CuInO_2$ and $CuScO_2$, the trend to be expected is not clear; however, both delafossites show similar lattice constants, while In^{3+} and Sc^{3+} ions also exhibit similar sizes according to [59]. The same can be said for $CuCrO_2$ and $CuFeO_2$ if we look for the Fe^{3+} size in the high-spin configuration. An unexpectedly low value of *a* compared to what could be intuitively expected is the one for $CuCoO_2$, which seems not to be an error of the simulation, since the experimental value [55] is very similar. However, it is consistent with the fact that the electronic structure calculated for this delafossite shows no spin polarization, indicating the Co^{3+} is in its low-spin configuration, and again the ion size of Co^{3+} in the low-spin configuration, as reported in [59], is very similar to the size of Al^{3+}, similar to the *a* lattice constant.

Therefore, the size of the metal ion, which is decisive to the *a* lattice constant, should play an important role in the conductivity of the delafossites, especially those with p-type

conductivity. This might be the explanation behind the fact that undoped $CuAlO_2$ has higher conductivity than both undoped $CuScO_2$ and $CuYO_2$ [16,28]. More discussion on the effect of the M cation size and *a* lattice constant on the conductivity can be found in [4,29] for some Mg-mixed Cu-based delafossites. It is of course not the only factor that contributes, with the covalency of the M-O bond being another important factor, as discussed in [19].

3.2. Hexagonal Structures

As mentioned before, in the hexagonal cells, the same layers of O-Cu-O dumbbells and M-centered octahedral are observed, but with an ABAB stacking pattern. It is expected, then, to find the lattice constant *a* to be practically identical between both phases, while the lattice constant *c* is expected to have a significantly lower value. The structure parameters found in our calculations, with some experimental values for comparison, are shown in Table 3.

Table 3. Lattice parameters *a* and *c* for the studied delafossite in the hexagonal structure (2H). The relaxed values from our simulations are compared to previous experimental results and the deviation from experimental values is expressed in %. When more than one experimental reference is shown, the deviation in the Table is the one with the highest absolute value.

	a (Å)		
	Relaxed value	Exp. references	Deviation from exp.
$CuAlO_2$	2.84	2.86 [54]	−0.7%
$CuGaO_2$	2.90		
$CuInO_2$	3.20		
$CuCoO_2$	2.83		
$CuScO_2$	3.13	3.22 [17,54]	−2.8%
$CuYO_2$	3.39	3.52 [60]	−3.7%
$CuCrO_2$	2.93	2.97 [61]	−1.3%
$CuFeO_2$	2.97		
	c (Å)		
	Relaxed value	Exp. references	Deviation
$CuAlO_2$	11.34	11.31 [54]	+0.27%
$CuGaO_2$	11.45		
$CuInO_2$	11.83		
$CuCoO_2$	11.298		
$CuScO_2$	11.52	11.41 [17,54]	+0.96%
$CuYO_2$	11.66	11.42 [60]	+2.1%
$CuCrO_2$	11.42	11.40 [61]	+0.18%
$CuFeO_2$	11.60		

The mentioned difference in *c* lattice constant between both phases is caused by the fact that a smaller distance is enough to represent the structure, because of the stacking sequence. Hence, important distances within the unit cell, such as the distance between two Cu neighbors in the *xy* plane (equal to the *a* lattice constant), the distance between Cu-O atoms in the O-Cu-O dumbbells, or the distance from cornered O to centered M in the octahedra are practically the same, as can be appreciated in Table 4.

Once more, the trend shown in the Cu-Cu distances (equal to the *a* lattice constant) is in agreement with the size of the trivalent metal ion. The same goes for the M-O distances, as expected. The O-Cu-O dumbbell distances, however, seem to be practically the same for all the structures, varying in a very short range of no more than 0.1 Å.

The relative stability of the two different phases is shown in Table 5. A negative Δ means the first structure has a lower energy, i.e., is the most stable one: the rhombohedral structure, in all our cases. However, the energy difference for all compounds falls under 0.3 eV, meaning both structures are relatively equally stable, and must be found indistinctly in nature [62].

Table 4. Comparative values for important interatomic distances within 3R and 2H phases of delafossite structure.

		Cu-Cu (Å)	Cu-O (Å)	M-O (Å)
$CuAlO_2$	3R	2.87	1.87	1.92
	2H	2.84	1.87	1.91
$CuGaO_2$	3R	2.97	1.85	1.995
	2H	2.90	1.83	1.97
$CuInO_2$	3R	3.28	1.84	2.19
	2H	3.20	1.84	2.16
$CuCoO_2$	3R	2.86	1.85	1.92
	2H	2.83	1.85	1.91
$CuScO_2$	3R	3.19	1.84	2.11
	2H	3.13	1.83	2.09
$CuYO_2$	3R	3.47	1.83	2.27
	2H	3.39	1.82	2.24
$CuCrO_2$	3R	2.98	1.85	1.99
	2H	2.93	1.84	1.97
$CuFeO_2$	3R	3.02	1.83	2.04
	2H	2.97	1.83	2.02

Table 5. Difference in basic state energy of rhombohedral vs. hexagonal structures for the studied delafossites E_{3R}-E_{2H}.

	$CuAlO_2$	$CuGaO_2$	$CuInO_2$	$CuCoO_2$	$CuScO_2$	$CuYO_2$	$CuCrO_2$	$CuFeO_2$
ΔE_0 (eV)	−0.26	−0.22	−0.21	−0.24	−0.298	−0.30	−0.29	−0.26

4. Electronic Structure

4.1. $CuAlO_2$, $CuGaO_2$ and $CuInO_2$

$CuAlO_2$ is probably the most extensively studied delafossite, with numerous theoretical and experimental studies. Some experimental works have reported a minimal value for the indirect bandgap in $CuAlO_2$ of 1.8 eV [3], very much deviated from the 3.4 eV we have obtained. This small value has been called into question [5,7], suggesting this highly underestimated measured bandgap could be related to some sort of defect. Several theoretical calculations (Table 6) give rise to a considerably larger indirect bandgap, supporting this consideration. Values range from 2.8 eV with an sX-LDA, which is expected to underestimate the gaps due to the LDA contribution, to 3.9 eV, the highest reported. In particular, three hybrid calculated values—including ours—seem to agree in a smaller range of values from 3.6 to 3.9 eV.

Table 6. Comparison of calculated bandgaps with previously reported bandgaps obtained with different simulation schemes.

Our simulations	
GGA	1.8
HSE06	3.4
Theoretical References	
GGA [5]	2.1
sX-LDA [12]	2.8
HSE03 [14]	3.1
G_0W_0 [14]	3.1
HSE06 [14]	3.6
B3LYP [5]	3.9

A detailed description of the electronic structure of the $CuAlO_2$ is shown in Figure 2a: HSE06 total and projected Density of States (DoS) as well as the band diagram with projected element contribution. While total DoS is shown in a black curve, element projected DoS is represented with color curves following the colors given to atomic species in Figure 1: red for Cu contributions, green for O contributions, and magenta for the contribution of the trivalent metal, Al in this case. In the bands diagram, every dot is a weighted mixture of these colors, where the projected contribution of each element to each point has been used as the weight.

The curves from DoS graphics are in excellent agreement with previous x-ray spectrum measures for $CuAlO_2$ [7]. The valence band edge shows a relatively weak—compared to its immediate neighbor—but well-defined peak dominated by Cu-3d states. This peak shows the red curve almost under the black one, which means the Cu contribution is dominant to the DoS, and the same can be appreciated by the almost pure red dots in the bands at the L-K line. A second and much stronger peak is observed next to it, also dominated by Cu-3d contributions mixed with O-2p states. This region's progressive fading from red to green in the band diagram accounts for the Cu-O mix. As the energies go deep into the band, a third broader and weaker region is observed, in which the O-2p contributions overcome the Cu presence. The dominant and wide region of green dots in the band suggests a wide dispersion of oxygen through the valence band. To find Al contributions, it is needed to look at the bottom of the band, where Al projected DoS is almost equal to Cu projected DoS in a fourth region, which corresponds in the band diagram to bands in which predominantly green dots turn to a darker color due to the magenta contribution.

The conduction band, on the other hand, starts with contributions mainly from Cu atoms and exhibits Al contributions near 10 eV. The valence band maximum (VBM) is located at the *L* point. The conduction band minimum is located at the Γ point and is constituted by Cu-3d states mixed with O-2p states. As CBM and VBM are located at different points of the Brillouin zone, the gap of the material is indirect.

For the $CuGaO_2$ (Figure 2b) and $CuInO_2$ (Figure 2c) delafossites, the electronic description is topographically quite similar, i.e., Cu dominated VB edge, the rest of the band showing the presence of Cu-3d mixed with O-2p states, with little to no contribution from the trivalent metal and O states, showing a wide dispersion in the region. A comparison of HSE06 calculated gaps for these three ternary oxides of group III-A and experimentally reported values can be found in Table 7.

Table 7. Calculated bandgaps and experimental references for group III-A delafossites.

	$CuAlO_2$	$CuGaO_2$	$CuInO_2$
Indirect gap	3.44	2.42	1.60
Direct gap, Γ	4.85	3.74	2.54
Direct gap, F	4.03	3.87	4.34
Direct gap, L	4.06	3.93	4.39
Experimental reference	3.5 [3] 3.60–3.94 [8]	3.6 [11]	3.9 [10]

Some general trends can be highlighted:

1. The three of them show an indirect fundamental bandgap.
2. Also, for the three of them, VBM is located at *L* point, while CBM is located at Γ point. The fundamental direct bandgap, i.e., the smallest direct gap, is located at Γ point for $CuGaO_2$ and $CuInO_2$ but at *L* point in $CuAlO_2$.
3. The fundamental bandgap, i.e., the indirect one, decreases from $CuAlO_2$ to $CuGaO_2$ and to $CuInO_2$. This trend is coherent with what is expected for group III-A containing semiconductors, but not with what has been experimentally measured.
4. The value of the bandgap at Γ point also decreases from $CuAlO_2$ to $CuGaO_2$ and to $CuInO_2$. This has been pointed out as the fundamental direct bandgap in previous reports [2] where matrix elements for direct transitions between band edge states have

been calculated, obtaining that transitions at Γ are forbidden, therefore explaining the inconsistency mentioned before between experimentally measured optical gaps and the fundamental gaps obtained in the calculations.

5. The bandgap at L point, in fact, slightly decreases from $CuAlO_2$ to $CuGaO_2$ but then increases to $CuInO_2$. This aligns with the experimental result. The same trend is observed at F point, and in general in the F-L line where band edges are closest to each other. The optical bandgap that is being measured must be related to this transition at the L point.
6. The width of the valence band decreases from $CuAlO_2$ to $CuGaO_2$ and to $CuInO_2$, which is coherent with experimental measurements [13].
7. The contribution of M^{III-A} states at the edge of the valence band is almost negligible for the three delafossites but becomes increasingly present at the bottom of the band from $CuAlO_2$ to $CuGaO_2$ and to $CuInO_2$, as can be observed in the coloring of the dots in the graphics. Actually, in $CuInO_2$, the contribution of In states begins to be appreciable around -5 eV, in the region dominated by O states.
8. The presence of states from the trivalent metal becomes increasingly important at lower energies, as well as in the conduction band, as seen in projected DoS from $CuAlO_2$ to $CuGaO_2$ and to $CuInO_2$.
9. The CBM at Γ is located at a lower energy from $CuAlO_2$ to $CuGaO_2$ and to $CuInO_2$.

The calculated band structure for $CuGaO_2$ with GGA, GGA + U, and HSE06 formalisms along the high-symmetry Γ-F-L-Γ points of the Brillouin zone is shown in Figure 3. It can be fairly appreciated that the increasing accuracy in calculations induces a vertical upward shift of the conduction band with respect to the Fermi Energy—which has been set equal to the Valence Band Maximum (VBM) and set to zero—with the consequent increase in bandgap value. However, despite this upward shift, the form of the conduction and valence bands at the edge are not appreciably modified. As a consequence, the Conduction Band Minimum (CBM) is located at Γ point in all three calculations, as well as the smallest direct gap, represented by arrows in the diagrams. The VBM—represented, as the CBM, by bigger dots in the pictures—is also located at the same point despite the approximation used: *L* point. Therefore, the fundamental bandgap is indirect in all three simulations. In summary, at least for the $CuM^{III-A}O_2$ delafossites, increasing accuracy does not change the band's description qualitatively.

However, some quantitative changes do happen when increasing accuracy. We previously mentioned the upward shift of the conduction band. The width of the valence band is also increased, deepening the lower states with the increase in accuracy from GGA to HSE, though the GGA + U shows a smaller bandwidth. This can be appreciated better by comparing the DoS and projected DoS for the three levels of calculation in Figure 4. However, it is possible to observe that despite the method, the valence band is dominated by Cu and O contributions, while the Ga contribution relies on the bottom of the band. In conclusion, despite quantitative differences, even at the GGA level, the electronic description of the material is qualitatively quite good. The same can be said for $CuAlO_2$ and $CuInO_2$.

Electronic Properties in Hexagonal Structures

The electronic properties of the hexagonal structures are substantially the same as in their rhombohedral counterparts. Indirect HSE bandgap values differ less than 1% for these structures, and the density of states follows very similar curves, as can be appreciated in Figure 5 for the group III-A ternary oxides previously analyzed.

Therefore, at least for applications depending only on electronic properties, the presence of either rhombohedral or hexagonal delafossite structures in a sample is indistinct. These similarities in electrical properties are quite an expected output due to the ones found in the geometry analyses of these two faces within the delafossite structure. If distances between atoms and angles of coordination are almost the same, bonds and electrical properties are expected to behave almost the same. This result has been previously discussed for $CuAlO_2$ [18] as well as for $CuCoO_2$ [62].

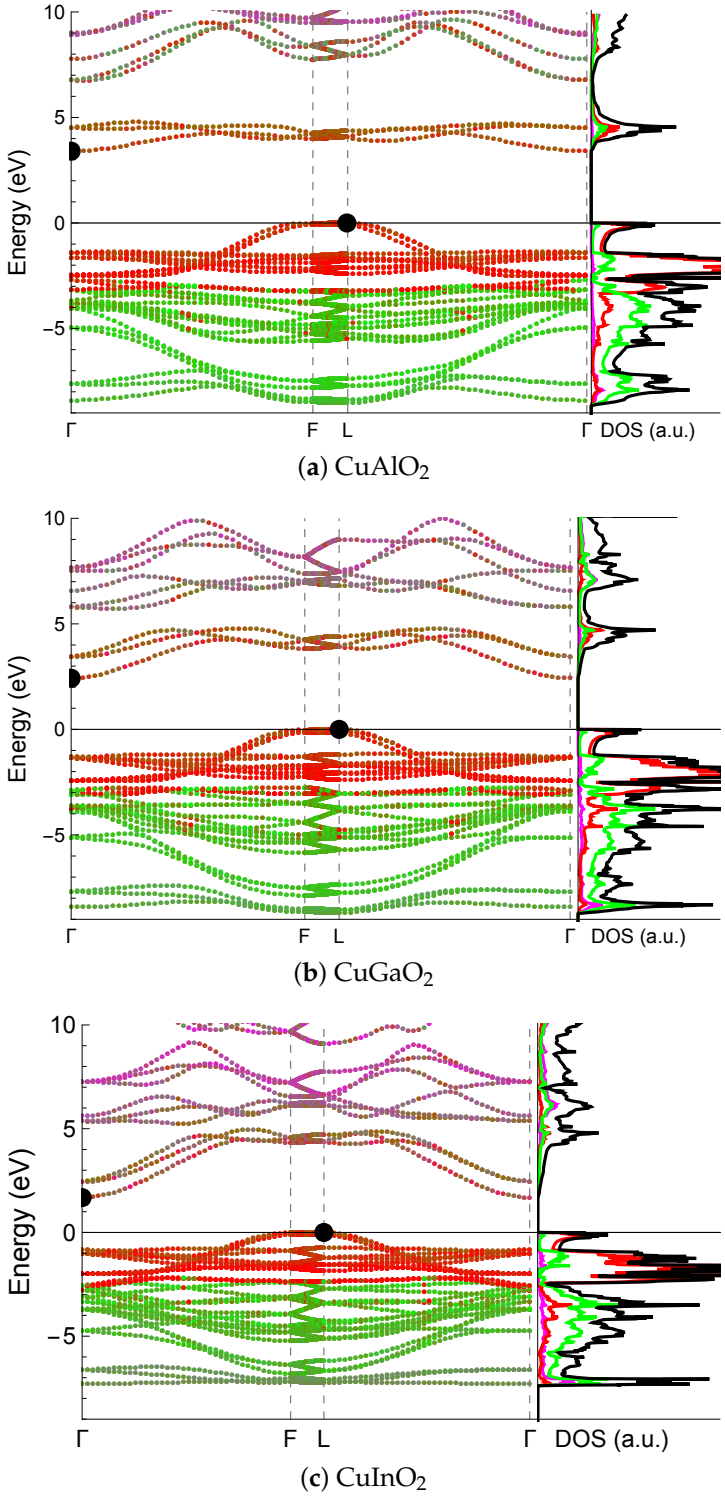

(**a**) $CuAlO_2$

(**b**) $CuGaO_2$

(**c**) $CuInO_2$

Figure 2. Band diagram and Density of States for the (**a**) $CuAlO_2$, (**b**) $CuGaO_2$, and (**c**) $CuInO_2$ delafossites with HSE functional. Energies are referred to with the Fermi energy (E_{Fermi} set to zero). Each dot color in the band diagram is a weighted mixture of red, green, and magenta, where the projected contribution of each element to the point has been used as the weight and the colors correspond as in the projected density with the ones in Figure 1. Bigger and black dots within the bands signal the VBM and CBM positions. The same color code has been used for the curves in DoS plots, while a black curve accounts for the total DoS.

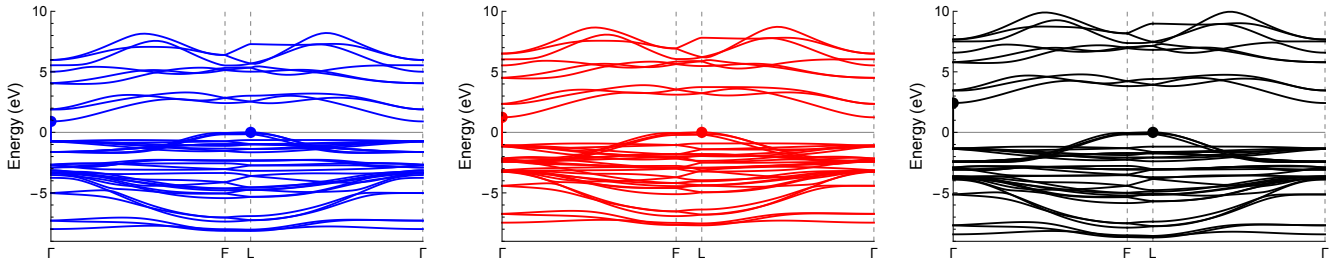

(**a**) GGA (**b**) GGA + U (**c**) HSE

Figure 3. Band structure calculations for $CuGaO_2$ at the GGA (**a**), GGA + U (**b**), and HSE06 (**c**) levels of calculations. The structure shown in all three band diagrams is qualitatively the same. With the increase in accuracy, however, the valence bandwidth increases. At the same time, the conduction band is vertically shifted upwards with the corresponding increase in the bandgap value. Nevertheless, the qualitative descriptions are appreciably the same, and important points VBM and CBM, as well as the position of the minimum direct gap, are at the same position in all three simulations.

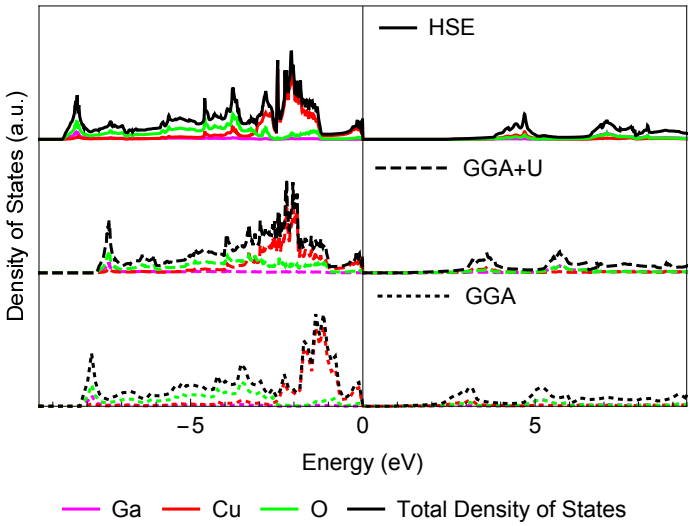

Figure 4. Density of States (DoS) and Projected DoS for each element in $CuGaO_2$ with GGA, GGA + U, and HSE functionals.

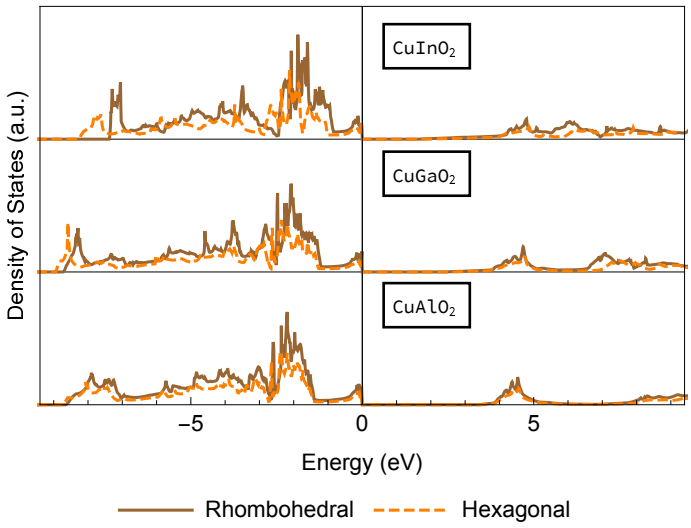

Figure 5. Total density of states for the studied $CuM^{III-A}O_2$ delafossites in rhombohedral $R\bar{3}m$ (continuous line) and hexagonal $P6_3/mmc$ (dashed line) structures with HSE hybrid functional.

4.2. $CuCoO_2$

Despite what was discussed in the previous section for the delafossites with metals of group III-A, in the description of delafossite oxides in which the valence electrons of the metal M are *d* electrons, the GGA methodology fails not just quantitatively. This is the case for the $CuCoO_2$, $CuScO_2$, $CuYO_2$, $CuCrO_2$, and $CuFeO_2$ structures. Taking $CuCoO_2$ to exemplify, Figure 6 shows the bands in the GGA (Figure 6a), GGA + U (Figure 6b), and HSE (Figure 6c) approximations. In the GGA, the bandgap is almost negligible, which means the energies of excited states are strongly underestimated. The $CuFeO_2$ shows the most inaccurate GGA calculation, leading to the band description of a conductor, i.e., zero gap.

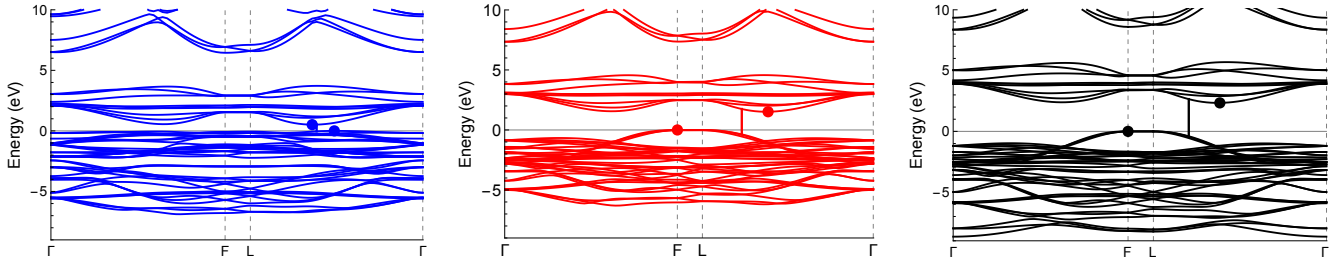

(**a**) GGA (**b**) GGA + U (**c**) HSE

Figure 6. Band structure calculations for $CuCoO_2$ at the (**a**) GGA, (**b**) GGA + U, and (**c**) HSE06 levels of calculations. The structure shown in (**a**) is notably different than the other two, meaning a failure of GGA calculations to represent Co-*d* states accurately.

However, more notably, there is a considerable difference in the form of the valence bands from GGA compared to GGA + U and HSE. Looking at the projected density of states in Figure 7, the problem in GGA calculation is the erroneous high energies of Co-3*d* states at the top of the band. The inclusion of the Hubbard term that matches the HSE density of states description corrects the location of these Co-3*d* states, moving them deeper into the band, and therefore, the GGA + U and HSE are qualitatively very much in agreement; however, the values of the excited states remain underestimated in GGA + U.

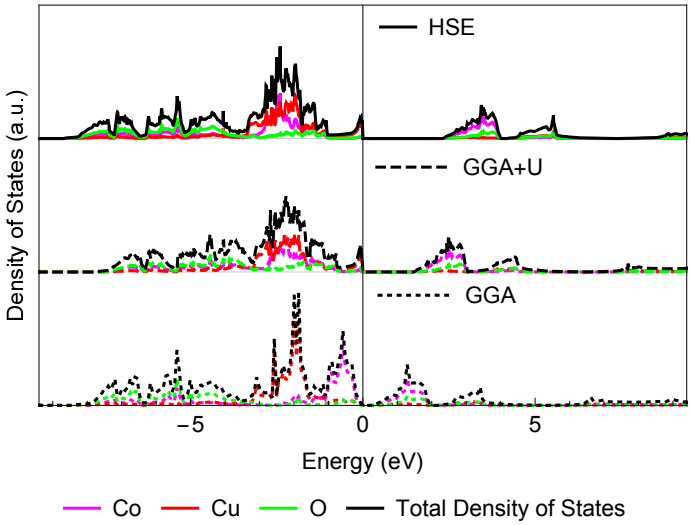

Figure 7. Density of States (DoS) and Projected DoS for each element in $CuCoO_2$ with GGA, GGA + U, and HSE functionals.

Figure 8 shows the band diagram and projected DoS for the $CuCoO_2$ delafossite obtained with HSE functionals. Spin-polarized calculations were performed, but up/down configurations produced the same result, thus confirming the Co^{3+} ion is in its low state and there are no unpaired electrons in the material. The VBM is at the *F* point, while the CBM is somewhere in the $L - \Gamma$ line. Therefore, the fundamental bandgap is indirect and

has a value of $E_{gap} = 2.34$ eV. The smallest direct bandgap is also located in the $L - \Gamma$ line, near the L point, and has a value of 3.40 eV, consistent with measured optical bandgaps in the range 3.4–3.9 [62,63].

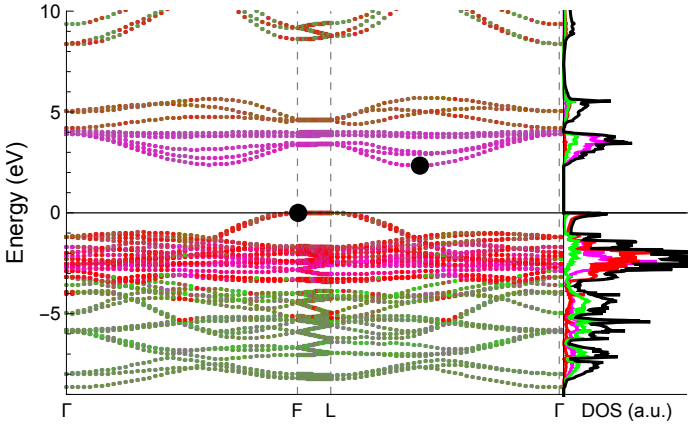

Figure 8. Band diagram and Density of States of $CuCoO_2$ with HSE functional. Dot colors within the band diagram stand for the contribution of each element to that singular k-point in the Brillouin zone.

The electronic structure shows a valence band edge dominated by Cu states. Like in the previously described delafossites, the first peak (from 0 to −1 eV) is energetically smaller than its immediate neighbor and is Cu-dominated. However, the second and higher peak, situated from −1 to −3 eV, exhibits a strong presence of Co-3*d* states, comparable to the Cu-3*d* contribution, even overcoming at some point the Cu contribution. From −3 eV and deeper, the main contribution is due to very delocalized O-2*p* states, mixed with Co contributions instead of Cu, as was the case for the M^{III-A} delafossites. On the other hand, the conduction band edge shows mainly Co-3*d* contributions mixed with a small O-2*p* presence and an almost negligible Cu presence in the first peak observed in the DoS diagram, approximately from 2.35 to 4 eV. The second and slightly smallest peak—from 4.2 to 6 eV—shows equal Co, Cu, and O contribution to the density of states.

4.3. $CuScO_2$ and $CuYO_2$

The delafossite compounds formed with Sc and Y in the place of the trivalent metal show a very notable difference compared with all other studied delafossites in this paper. As can be appreciated in Figure 9, these two band diagrams show that $CuScO_2$ and $CuYO_2$ have a direct bandgap at F point, as has been previously reported [12,64]. On the other hand, as this transition at F is symmetry-allowed, a good agreement between the calculated direct bandgap and the experimental measured optical gap is expected. Our 3.5 eV is only 0.2 eV overestimated to the measured 3.3 eV gap for $CuScO_2$ [65], while our 3.9 eV calculated bandgap for $CuYO_2$ is also slightly overestimated to the measured 3.5 eV for this delafossite [66].

An important difference in the electronic structure when compared with the previously described delafossites ($CuM^{III-A}O_2$ and $CuCoO_2$) lies in the bottom of the conduction band. While the $CuM^{III-A}O_2$ structures showed the edge of the conduction band filled with Cu-*d* states hybridized with O-*p* states and the $CuCoO_2$ conduction band edge was filled with Co-*d* states also hybridized with O-*p* states, these two $CuM^{III-B}O_2$ exhibit a conduction band with an important and almost exclusive contribution of Sc/Y-*d* states, as can be appreciated in the almost pure magenta coloring of the dots in the conduction band of the band diagrams in Figure 9. In $CuScO_2$, the conduction band has no definite and separated peaks, but a wide band with mainly Sc-*d* states, followed by a smaller contribution of Cu-*d* states mixed with O-2*p* with a high dispersion, as can also be seen in the curves of DoS on the right side of Figure 9a. In $CuYO_2$, the conduction band edge shows a first peak with equal contribution of Y-*d* states with the mixture of Cu-*d* and O-*p* states, as

shown by almost overlapping curves from 4 to 5 eV on the right side of Figure 9b, followed by a wide band, as in the case of Sc delafossite, with almost exclusively Y-*d* contribution.

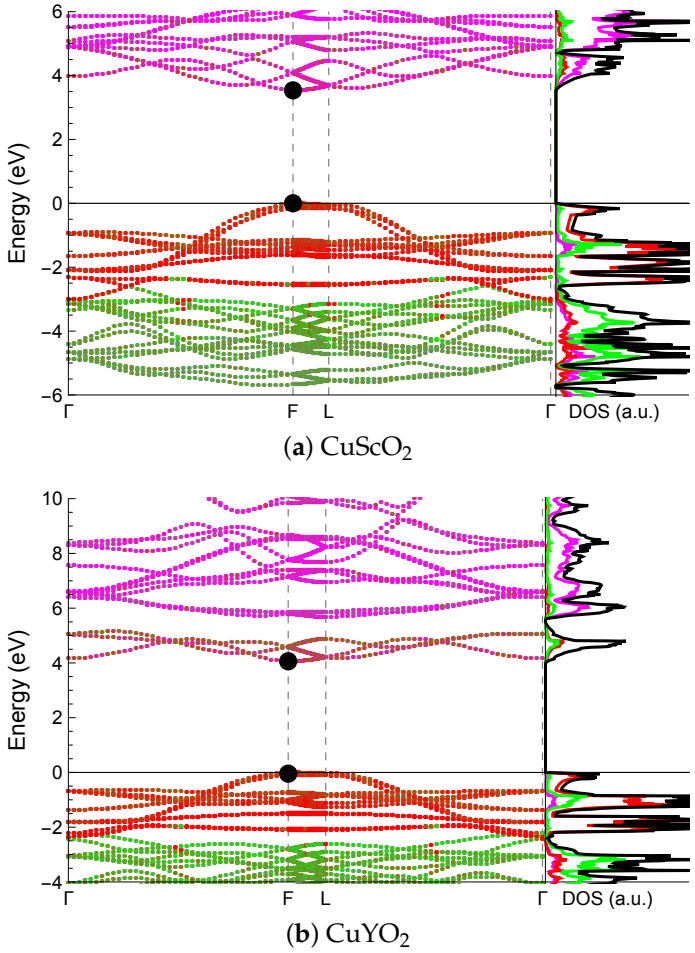

Figure 9. Bands diagram and Density of States (DoS) for the (**a**) $CuScO_2$ and (**b**) $CuYO_2$ delafossites with HSE functional. Both oxides show a direct bandgap at F.

4.4. $CuCrO_2$ and $CuFeO_2$

For the $CuCrO_2$ and $CuFeO_2$, as both Fe—in its high-spin configuration—and Cr atoms present unpaired electrons, spin-polarized calculations were performed. In Figure 10 HSE DoS are represented for these materials, in which positive curves account for Spin-Up contributions to the DoS and negative curves for the Spin-Down.

The electronic structure of $CuCrO_2$ can be appreciated in Figure 10a. It is similar to the ones observed in previous delafossite structures and quite similar in both Up/Down configurations. The edge of the valence band belongs to the Up configuration. It presents a first peak—from 0 to −1 eV—of mainly Cu contributions, separated from the second and higher peak—from −1 to −3.5 eV—which exhibits mostly Cr contributions, with mixed Cu-O states. On the downside, the first peak is almost identical to its corresponding Up configuration, but the second one has almost no Cr contribution, showing an important Cu presence and a relatively small O presence. From −3.5 eV and deeper into the band, both sides show a wide dispersion of O states, being almost the only contribution in the down configuration, while the up configuration also shows Cr and smaller but appreciable Cu contributions. On the other hand, the conduction band starts growing both in the Up and Down configuration with mainly Cr contributions, mixed in the Up configuration with O states, but being almost the only contribution on the downside.

A different scenario is found by inspecting the electronic structure of $CuFeO_2$ in Figure 10b. The valence band edge is very similar in energy for both Up and Down

configurations, and exhibits mainly Cu contributions, as all described structures before. This dominant Cu contribution remains through a wide range of energy into the band—reaching −3 eV in the Down configuration and −3.5 eV in the Up part—with a very discrete contribution of Fe states. From this point and deeper, on the downside, the valence band DoS is almost solely O contributions, while in the Up configuration, a strong Fe contribution appears around −7 eV. This is coherent with previously reported DoS [34,35]. The conduction band starts growing on the downside with a strong contribution of Fe states, from 1.3 to 2 eV, and a second Fe-dominant peak from 2.4 to 3.7 eV. The Down-spin states that pair with the 5 unpaired *d*-electrons of Fe are responsible for the small gap found in this delafossite, the smallest within the studied delafossites in this paper.

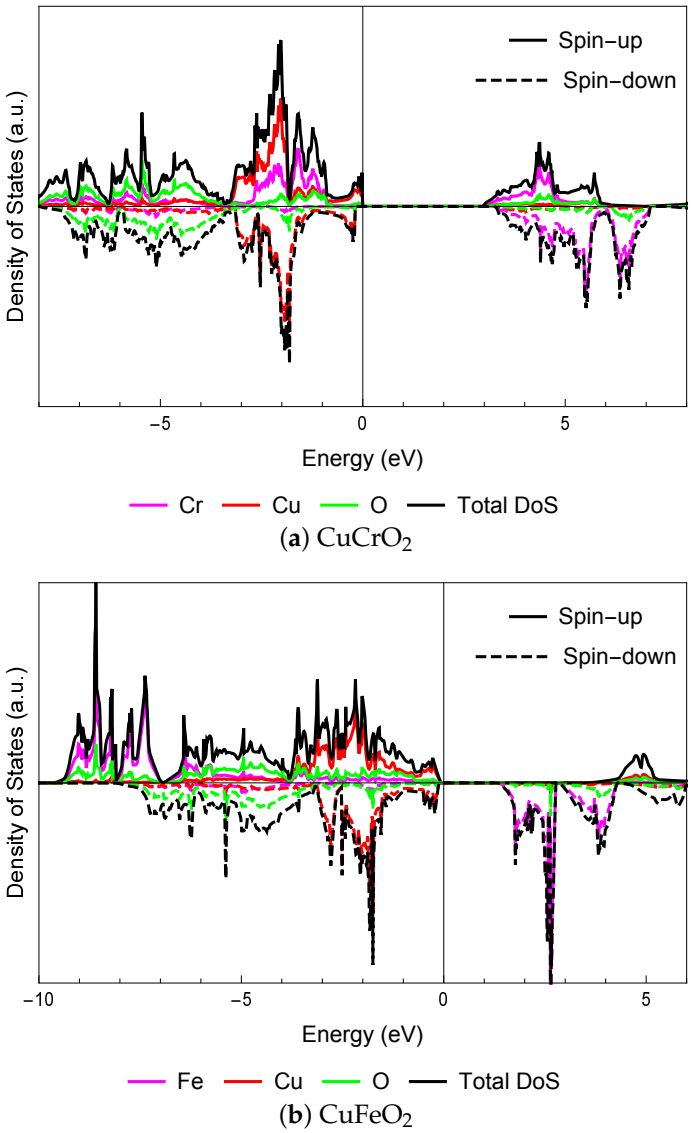

Figure 10. Density of States (DoS) for the (**a**) $CuCrO_2$ and (**b**) $CuFeO_2$ delafossites with HSE functional.

5. Mixed Structures

To explore the effects of the substitution of one of the trivalent metals in the delafossite compounds, we have studied the substitution of one of the trivalent metals (Al, Ga, In, Co, Sc, Y, Cr, Fe), having as possible substitutes the same set of metals. Changes in geometry, gap value, and electronic structure have been analyzed in $CuM_xN_{1-x}O_2$ structures, where $x = 1/3$. In this section, as for the pure delafossites, structural results arise from GGA calculations while bandgaps were obtained in HSE simulations.

The inclusion of ions with a larger radius in a delafossite with a smaller M metal is expected to increase both *a* and *c* parameters, as well as the cell volume. However, in general, we have observed that while the parameter *a* increases with the increase in a larger metal in the composition, it is not the case for parameter *c*. This can be fairly appreciated in Figure 11 for a selection of these mixed structures.

As the amount of Ga increases in Figure 11a, the parameter *a* also increases, suggesting a linear tendency. The same can be said for the amount of In in Figure 11b, In in Figure 11c, Sc in Figure 11d, Fe in Figure 11e, or Cr in Figure 11f. For every mix, we have calculated only four structures, and a rigorous fit can not be performed with such a small amount of data points.

The case is completely different for the cell parameter *c*. It can be appreciated in the inset plots in Figure 11. In Figure 11a–c, this parameter also seems to increase with the increase in the amount of larger metal. In these three examples, the substituted metal has a very similar electronic composition as the one to be substituted, since Al, Ga, In belong to the same group in the periodic table. But in all other cases, it is fairly appreciated that there is no clear dependency of *c* on the amount of substituted metal, since the dispersion of the four points is notable. This behavior was also found previously [40] for $CuFe_xGa_{1-x}O_2$. The referred study concluded that the *c* parameter is almost independent of the concentration of the substituted cation. A possible explanation is that the strong repulsion of the M cations in the *ab* plane affects the MO_6 octahedra, rearranging the oxygen atom positions. As the M cation becomes larger, the M–O distance increases, but the O–O contact distance varies only slightly, and therefore, there is little impact on the *c* cell parameter.

The complete set of values for the geometry of these structures can be found in Table 8.

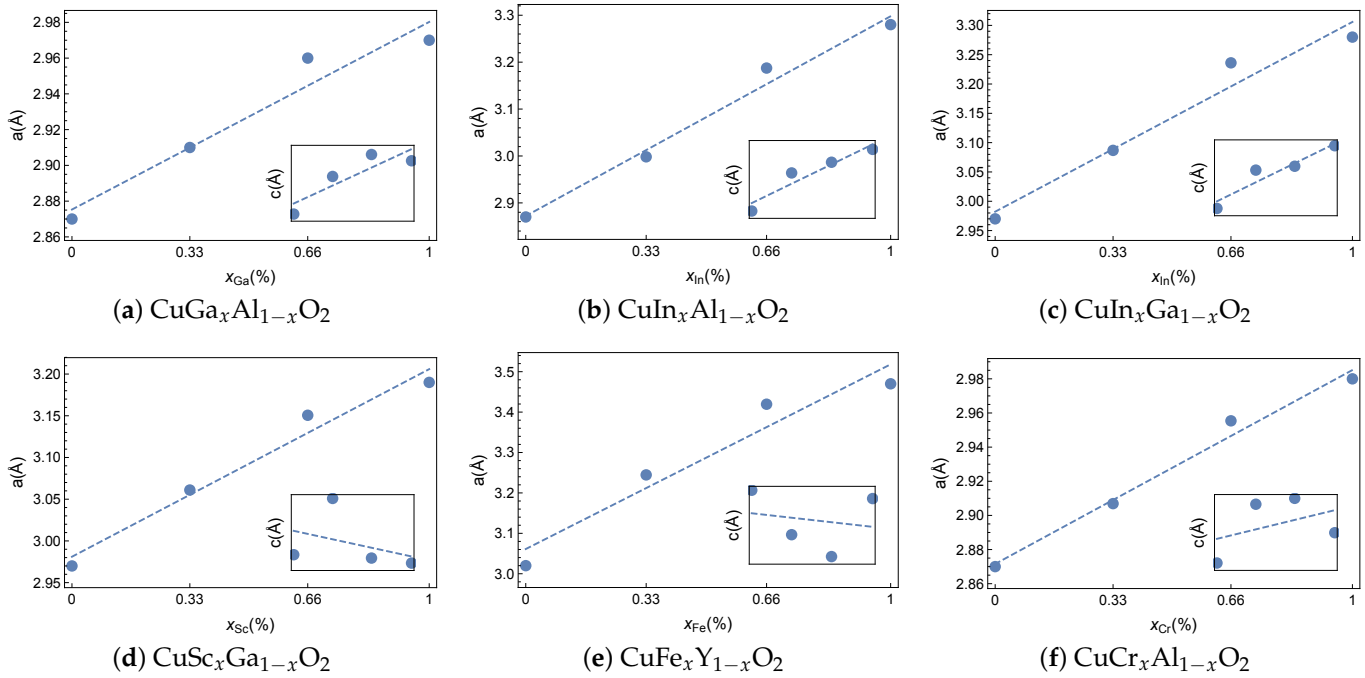

(**a**) $CuGa_xAl_{1-x}O_2$ (**b**) $CuIn_xAl_{1-x}O_2$ (**c**) $CuIn_xGa_{1-x}O_2$

(**d**) $CuSc_xGa_{1-x}O_2$ (**e**) $CuFe_xY_{1-x}O_2$ (**f**) $CuCr_xAl_{1-x}O_2$

Figure 11. Cell parameter *a* as a function of *x*, the amount of substituted metal in some mixed delaffosites. On insets, same comparison with cell parameter *c*.

Bandgap values have been calculated and the DoS structures analyzed. In general, it is impossible to find any clear trend in the behavior of the bandgap values, as was true for the geometry. An exception to this is the $CuGa_xAl_{1-x}O_2$ case. As can be appreciated in Figure 12a, the gaps seem to follow a linear decrease with the increase in Ga concentration. This is not surprising, since in both $CuAlO_2$ and $CuGaO_2$ electronic structures, the states of the trivalent metal are very deep in the valence band, and very high in energy in the conduction band. All the interaction near the gap is due to Cu atoms and the tightness

of the bond shall only be determined by its Cu-Cu distance. As mentioned before, the structure increases linearly in *a* and *c* for these delafossites, thus causing the electrons to feel a softer potential and be less tightly bonded to the Cu atoms. A second exception is found by inspecting every delafossite that includes Fe in the substitution. The Fe-states appear so energetically low in the conduction band that the inclusion of any Fe atom causes the bandgap to exhibit very similar values, despite which was the host delafossite (Figure 12b).

Table 8. Lattice constant *a* and *c* (in Å) for $CuM_{1/3}N_{2/3}O_2$ delafossite structures obtained with GGA functional. In the diagonal, the values of the pure delafossites previously discussed are shown.

a(Å) c(Å)	-$Al_{2/3}$	-$Ga_{2/3}$	-$In_{2/3}$	-$Co_{2/3}$	-$Sc_{2/3}$	-$Y_{2/3}$	-$Cr_{2/3}$	-$Fe_{2/3}$
$Al_{1/3}$-	**2.87** **17.05**	2.96 17.24	3.19 17.50	2.86 17.01	3.11 17.20	3.35 17.22	2.96 17.16	2.96 17.33
$Ga_{1/3}$-	2.91 17.17	**2.97** **17.22**	3.24 17.49	2.91 17.04	3.15 17.22	3.39 17.199	2.97 17.13	3.02 17.34
$In_{1/3}$-	2.998 17.40	3.09 17.47	**3.28** **17.62**	3.00 17.19	3.25 17.29	3.48 17.23	3.13 17.27	3.10 17.40
$Co_{1/3}$-	2.87 17.04	2.96 17.16	3.20 17.33	**2.87** **16.96**	3.12 17.05	3.37 16.98	2.96 17.08	2.96 17.26
$Sc_{1/3}$-	2.97 17.20	3.06 17.29	3.29 17.40	2.98 17.02	**3.19** **17.21**	3.44 17.15	3.07 17.12	3.098 17.26
$Y_{1/3}$-	3.09 17.31	3.27 17.31	3.42 17.35	3.12 16.98	3.33 17.17	**3.47** **17.31**	3.099 17.16	3.24 17.18
$Cr_{1/3}$-	2.91 17.15	2.96 17.18	3.24 17.36	2.90 17.05	3.15 17.12	3.39 17.06	**2.98** **17.10**	3.02 17.28
$Fe_{1/3}$-	2.898 17.24	2.97 17.29	3.26 17.42	2.90 17.15	3.17 17.19	3.42 17.10	3.01 17.21	**3.02** **17.34**

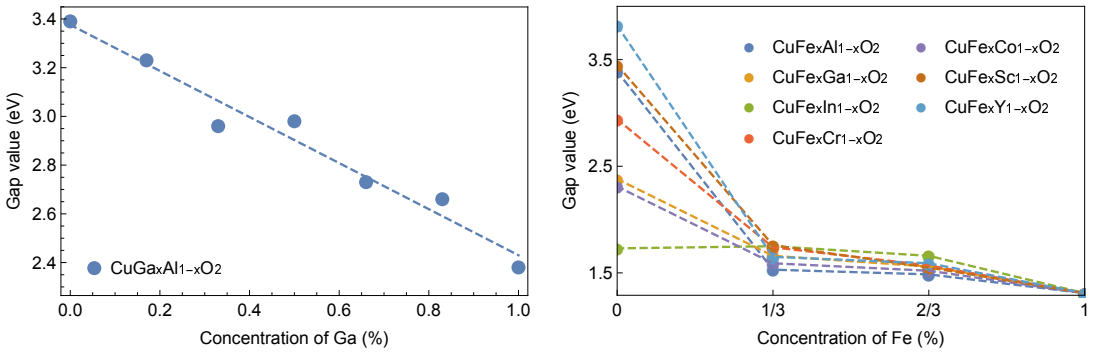

(**a**) $CuGa_xAl_{1-x}O_2$ (**b**) $CuFe_xM_{1-x}O_2$

Figure 12. Bandgap values vs. percentage of substitution for (**a**) $CuGa_xAl_{1-x}O_2$ and (**b**) $CuFe_xM_{1-x}O_2$, where M represents all the species we have tested in this work.

However, apart from these two mentioned examples, there is no clear trend in the gap values that can be analyzed. The complete set of HSE values for these structures can be found in Table 9.

Table 9. Indirect bandgap values (in eV) with HSE functionals for $CuM_{1/3}N_{2/3}O_2$ delafossite structures. Arrows indicate whether the gap belongs to up/down configurations in spin-polarized calculations for structures containing Cr and Fe atoms.

Bandgap (eV)	-$Al_{2/3}$	-$Ga_{2/3}$	-$In_{2/3}$	-$Co_{2/3}$	-$Sc_{2/3}$	-$Y_{2/3}$	-$Cr_{2/3}$	-$Fe_{2/3}$
$Al_{1/3}$-	**3.39**	2.74	1.90	2.45	3.38	2.90	$3.17^{\uparrow}$	$1.49^{\downarrow}$
$Ga_{1/3}$-	2.96	**2.38**	1.88	2.38	2.48	1.72	$2.96^{\downarrow}$	$1.56^{\downarrow}$
$In_{1/3}$-	2.04	1.99	**1.73**	2.17	2.16	1.96	$2.18^{\uparrow}$	$1.66^{\downarrow}$
$Co_{1/3}$-	2.58	2.47	1.95	**2.31**	2.06	1.53	$2.34^{\uparrow}$	$1.52^{\downarrow}$
$Sc_{1/3}$-	3.17	2.48	1.83	2.28	**3.45**	3.64	$2.99^{\uparrow}$	$1.55^{\downarrow}$
$Y_{1/3}$-	2.65	2.36	1.80	2.11	3.54	**3.82**	$2.87^{\uparrow}$	$1.59^{\downarrow}$
$Cr_{1/3}$-	$3.29^{\downarrow}$	$2.67^{\downarrow}$	$1.82^{\downarrow}$	$2.32^{\uparrow}$	$3.02^{\uparrow}$	$2.66^{\uparrow}$	**2.94**$^{\uparrow}$	$1.57^{\downarrow}$
$Fe_{1/3}$-	$1.53^{\downarrow}$	$1.66^{\downarrow}$	$1.75^{\downarrow}$	$1.59^{\downarrow}$	$1.76^{\downarrow}$	$1.65^{\downarrow}$	$1.74^{\downarrow}$	**1.31**$^{\downarrow}$

6. Statistical Models and Machine Learning

The computational effort to calculate HSE bandgaps can be, as has been said, demanding in terms of time and memory needed. This is especially true for structures with relative compositions M/N different than 1/3 (or 2/3). Therefore, we discuss the use of statistical models and techniques based on machine learning to predict HSE bandgaps given the structural information of the material and its GGA calculated bandgap. A step of ab initio calculation is still needed, but the cost of a calculation with a GGA functional is far less expensive than those using HSE functionals.

To use machine learning techniques or other statistical models, a numerical way of fully describing structures is needed. These numerical representations are the descriptors, which must be invariant to symmetry operations, complete and unique, meaning able to distinguish between any two different structures [67]. The descriptor for which the best performance has been obtained in our current work is the sine matrix [68], consisting of an *ansatz* that mimics the periodicity and the basic features of the elements in the Ewald sum matrix for a periodic system, using a sine function of the crystal coordinates of the atoms.

Apart from the sine matrix description, some other parameters of chemical nature have been added to the descriptor: the covalent radius, electronegativity, and ionization potential of the metal cations occupying M, N positions. Additionally, given the aim of this approach, the GGA results have been added as well as an extra feature of the descriptor. The featurization of the structures was carried out with the Python libraries matminer [69] and smact [70–72]. This featurization was performed for structures with 24 atoms ($2 \times 1 \times 1$ rhombohedral supercells), the ones that will be used to test results for new unbalanced configurations, but 12-atom structures (the cells used to model all results in previous sections) were processed as well, in order to check the consistency of results. We ensured that identical models were trained separately for both sets of structures of 12- and 24-atom unit cells, and the average deviation of bandgap results between both was 56 meV, a very small value in terms of bandgaps of semiconductors in the range between approximately 2 and 4 eV. This result suggests that scaling up to even larger unit cells should also yield consistent results.

Regarding the model, because of the limited number of structures considered relevant to describe this family of compounds with delafossite structure, high-complexity models like neural networks, which require large training sets, were automatically discarded even for initial evaluation. Beyond those, other smaller models have been tested, like simple regularized and non-regularized linear regressors, support vector regressors, and gradient-boosting regressors based on decision trees. For all of them, a proper search of optimal hyperparameters has been performed. The best results were achieved with a

LASSO regressor (linear regressor with L1 regularization) with an alpha parameter for the regularization of 0.01.

For the evaluation of the models and descriptors, a standard train–test splitting was implemented within a leave-one-group-out cross-validation scheme [73], using the 64 structures of 12 atoms described in Section 5. The size of the test is equal to the square root of the total number of compounds in all the cases, with the training set made up of the remaining compounds. Groups for cross-validation were chosen so the balance between training and test sets was always maintained, meaning that the number of compounds in the set with any of the different metal cations studied was always the same. Following that scheme, average and best results between the series of folds in the cross-validation are here presented in Table 10, which shows main performance evaluation metrics like the mean absolute error (MAE) and maximum error (ε_{max}) between the predicted and DFT calculated results. According to common procedures of model evaluation, the errors presented in the table have been calculated only for the test sets. The results for the best fold are also presented in Figure 13a. Given that all the Fe compounds present a GGA bandgap of 0, an analogous study was performed without including these compounds. Results for the sets without Fe compounds are also presented in the table, for comparison purposes, as it is clearly seen how the performance metrics improve filtering them.

Table 10. Performance metrics comparing statistically predicted and DFT calculated bandgaps for the different sets of structures in eV.

	Average of Folds		**Best Fold**	
	MAE	ε_{max}	**MAE**	ε_{max}
Whole set	0.162	0.330	0.078	0.165
Set without Fe	0.130	0.288	0.077	0.166

Average results show that this method yields approximate results, which certainly should not be taken as definitive nor exact. However, the aim of this process is not to obtain the most accurate bandgap values but to obtain results within an acceptable range of accuracy that allow us to preselect which compositions would be the most suitable for our purposes.

With the choice of the descriptor and the model already defined, the same process has been followed to evaluate the performance of new structures, with the same crystal structure and same set of species in N, M positions but with relative concentration ratios of metal cations not used for the training of the model. A set of eight new structures ($CuAl_{1/6}Ga_{5/6}O_2$, $CuAl_{1/2}Ga_{1/2}O_2$, $CuAl_{5/6}Ga_{1/6}O_2$, $CuAl_{5/6}In_{1/6}O_2$), $CuAl_{5/6}Cr_{1/6}O_2$, $CuAl_{1/6}Co_{5/6}O_2$, $CuGa_{1/2}In_{1/2}O_2$, $CuSc_{5/6}Y_{1/6}O_2$) have been used as the test set, using the sixty-four original compounds as the training set in this case. These results, with the corresponding performance metrics (MAE, ε_{max} and r2), are presented in Figure 13b. Slightly higher errors are obtained in this case, compared with those obtained for the original compounds; however, they are very similar, considering that we are predicting concentration ratios not used to train the model. These results, with errors that fall within a tolerance margin of $+/-0.2$ eV, could still be of perfect use for preselecting compounds based on this property with high levels of confidence.

These results prove that this machine learning-based approach could be extremely useful to further explore this family of compounds efficiently and affordably, especially considering the titanic computational cost of running HSE calculations for several of these compounds that requires a description with large unit cells and the very inaccurate results obtained with GGA functionals. Indeed, a similar approach could be used as well to predict other properties of interest to sketch a map of properties to efficiently select the most promising compounds within the compositional landscape of this family of compounds, given those properties can be directly inferred from DFT calculations like the ones performed in this work.

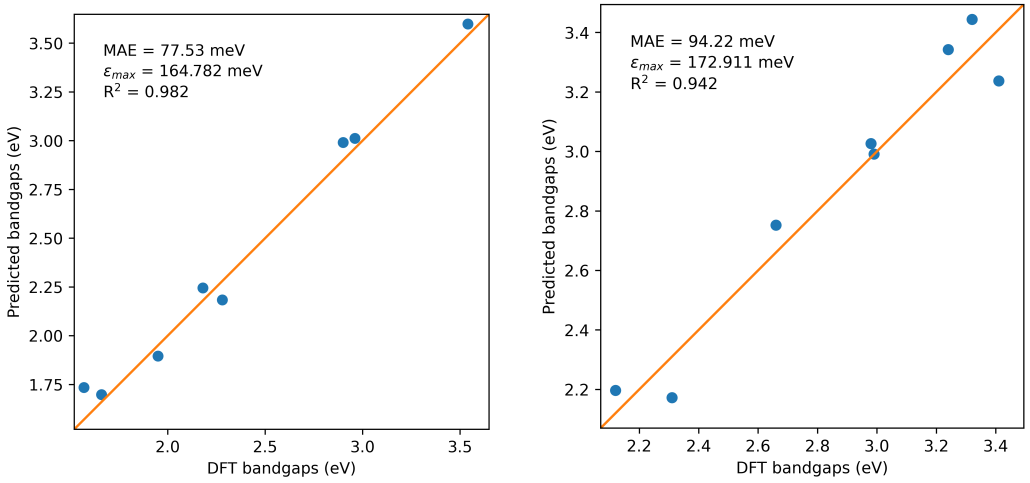

Figure 13. Comparison of results predicted with the models and those calculated with DFT (**a**) for the original set of structures in the fold of the cross-validation which yields the best metrics and (**b**) for the additional set of compounds with new concentration ratios.

7. Conclusions

A study with several $CuMO_2$ compounds with delafossite structure has been carried out, using DFT and different levels of accuracy in the representation of the exchange correlation functional. The structural characterization for both reported phases has been compared to experimental results, finding excellent agreement. For the electronic properties, it has been found that even GGA simulations yield qualitatively acceptable results for the compounds with a metal from group III-A occupying the M site, but fail to represent other compounds. For the delafossites with the rest of the studied elements, simulations with GGA + U were found to be able to qualitatively represent the electronic properties of the materials, with a proper selection of the U parameter. All of the materials studied exhibited indirect bandgaps except for the ones containing Sc and Y on the M site. Mixed structures were also analyzed, and machine learning techniques were tested and showed the ability to infer HSE bandgap values with a reasonable tolerance margin, even for structures with a larger number of atoms than those calculated with DFT.

Author Contributions: Conceptualization, J.C.T. and P.P.; Investigation, J.C.T. and P.S.-P.; Methodology, J.C.T., P.S.-P. and P.P.; Supervision, P.P.; Writing—original draft, J.C.T. and P.S.-P.; Writing—review and editing, J.C.J.-S., P.W. and P.P. All authors have read and agreed to the published version of the manuscript.

Funding: This work has been sponsored by the Project CEOTRES-CM (Y2020/EMT-6419) funded by the Comunidad de Madrid.

Data Availability Statement: The original contributions presented in the study are included in the article material; further inquiries can be directed to the corresponding author/s.

Acknowledgments: The authors gratefully acknowledge the Universidad Politécnica de Madrid (www.upm.es) for providing computing resources on Magerit Supercomputer.

Conflicts of Interest: The authors declare no conflicts of interest. The funders had no role in the design of the study; in the collection, analyses, or interpretation of data; in the writing of the manuscript; or in the decision to publish the results.

References

1. Kawazoe, H.; Yasukawa, M.; Hyodo, H.; Kurita, M.; Yanagi, H.; Hosono, H. P-type electrical conduction in transparent thin films of $CuAlO_2$. *Nature* **1997**, *389*, 939–942. [CrossRef]
2. Nie, X.; Wei, S.H.; Zhang, S.B. Bipolar Doping and Band-Gap Anomalies in Delafossite Transparent Conductive Oxides. *Phys. Rev. Lett.* **2002**, *88*, 066405. [CrossRef] [PubMed]

3. Yanagi, H.; Inoue, S.i.; Ueda, K.; Kawazoe, H.; Hosono, H.; Hamada, N. Electronic structure and optoelectronic properties of transparent p-type conducting $CuAlO_2$. *J. Appl. Phys.* **2000**, *88*, 4159–4163. [CrossRef]
4. Nagarajan, R.; Duan, N.; Jayaraj, M.; Li, J.; Vanaja, K.; Yokochi, A.; Draeseke, A.; Tate, J.; Sleight, A. p-Type conductivity in the delafossite structure. *Int. J. Inorg. Mater.* **2001**, *3*, 265–270. [CrossRef]
5. Robertson, J.; Peacock, P.; Towler, M.; Needs, R. Electronic structure of p-type conducting transparent oxides. *Thin Solid Films* **2002**, *411*, 96–100. [CrossRef]
6. Shannon, R.D.; Rogers, D.B.; Prewitt, C.T.; Gillson, J.L. Chemistry of noble metal oxides. III. Electrical transport properties and crystal chemistry of ABO2 compounds with the delafossite structure. *Inorg. Chem.* **1971**, *10*, 723–727. [CrossRef]
7. Aston, D.J.; Payne, D.J.; Green, A.J.H.; Egdell, R.G.; Law, D.S.L.; Guo, J.; Glans, P.A.; Learmonth, T.; Smith, K.E. High-resolution x-ray spectroscopic study of the electronic structure of the prototypical *p*-type transparent conducting oxide $CuAlO_2$. *Phys. Rev. B* **2005**, *72*, 195115. [CrossRef]
8. Banerjee, A.N.; Chattopadhyay, K.K. Size-dependent optical properties of sputter-deposited nanocrystalline p-type transparent $CuAlO_2$ thin films. *J. Appl. Phys.* **2005**, *97*, 084308. [CrossRef]
9. Xiong, D.; Zeng, X.; Zhang, W.; Wang, H.; Zhao, X.; Chen, W.; Cheng, Y.B. Synthesis and Characterization of $CuAlO_2$ and $AgAlO_2$ Delafossite Oxides through Low-Temperature Hydrothermal Methods. *Inorg. Chem.* **2014**, *53*, 4106–4116. [CrossRef] [PubMed]
10. Yanagi, H.; Hase, T.; Ibuki, S.; Ueda, K.; Hosono, H. Bipolarity in electrical conduction of transparent oxide semiconductor CuInOwith delafossite structure. *Appl. Phys. Lett.* **2001**, *78*, 1583–1585. [CrossRef]
11. Ueda, K.; Hase, T.; Yanagi, H.; Kawazoe, H.; Hosono, H.; Ohta, H.; Orita, M.; Hirano, M. Epitaxial growth of transparent p-type conducting $CuGaO_2$ thin films on sapphire (001) substrates by pulsed laser deposition. *J. Appl. Phys.* **2001**, *89*, 1790–1793. [CrossRef]
12. Gillen, R.; Robertson, J. Band structure calculations of $CuAlO_2$, $CuGaO_2$, $CuInO_2$, and $CuCrO_2$ by screened exchange. *Phys. Rev. B* **2011**, *84*, 035125. [CrossRef]
13. Shin, D.; Foord, J.S.; Payne, D.J.; Arnold, T.; Aston, D.J.; Egdell, R.G.; Godinho, K.G.; Scanlon, D.O.; Morgan, B.J.; Watson, G.W.; et al. Comparative study of bandwidths in copper delafossites from x-ray emission spectroscopy. *Phys. Rev. B* **2009**, *80*, 233105. [CrossRef]
14. Trani, F.; Vidal, J.; Botti, S.; Marques, M.A.L. Band structures of delafossite transparent conductive oxides from a self-consistent *GW* approach. *Phys. Rev. B* **2010**, *82*, 085115. [CrossRef]
15. Yu, M.; Draskovic, T.I.; Wu, Y. Cu(i)-based delafossite compounds as photocathodes in p-type dye-sensitized solar cells. *Phys. Chem. Chem. Phys.* **2014**, *16*, 5026–5033. [CrossRef]
16. Godinho, K.; Morgan, B.; Allen, J.; Scanlon, D.; Watson, G. Chemical bonding in copper-based transparent conducting oxides: $CuMO_2$ (M = In, Ga, Sc). *J. Phys. Condens. Matter Inst. Phys. J.* **2011**, *23*, 334201. [CrossRef] [PubMed]
17. Li, J.; Yokochi, A.F.; Sleight, A.W. Oxygen intercalation of two polymorphs of $CuScO_2$. *Solid State Sci.* **2004**, *6*, 831–839. [CrossRef]
18. Buljan, A.; Alemany, P.; Ruiz, E. Electronic Structure and Bonding in $CuMO_2$ (M = Al, Ga, Y) Delafossite-Type Oxides: An Ab Initio Study. *J. Phys. Chem. B* **1999**, *103*, 8060–8066. [CrossRef]
19. Scanlon, D.O.; Godinho, K.G.; Morgan, B.J.; Watson, G.W. Understanding conductivity anomalies in CuI-based delafossite transparent conducting oxides: Theoretical insights. *J. Chem. Phys.* **2010**, *132*, 024707. [CrossRef]
20. Zheng, S.; Jiang, G.; Su, J.; Zhu, C. The Structural and Electrical Property of $CuCr_{1-x}Ni_xO_2$ Delafossite Compounds. *Mater. Lett.* **2006**, *60*, 3871–3873. [CrossRef]
21. Arnold, T.; Payne, D.J.; Bourlange, A.; Hu, J.P.; Egdell, R.G.; Piper, L.F.J.; Colakerol, L.; De Masi, A.; Glans, P.A.; Learmonth, T.; et al. X-ray spectroscopic study of the electronic structure of $CuCrO_2$. *Phys. Rev. B* **2009**, *79*, 075102. [CrossRef]
22. Yokobori, T.; Okawa, M.; Konishi, K.; Takei, R.; Katayama, K.; Oozono, S.; Shinmura, T.; Okuda, T.; Wadati, H.; Sakai, E.; et al. Electronic structure of the hole-doped delafossite oxides $CuCr_{1-x}Mg_xO_2$. *Phys. Rev. B* **2013**, *87*, 195124. [CrossRef]
23. Dunlap-Shohl, W.A.; Daunis, T.B.; Wang, X.; Wang, J.; Zhang, B.; Barrera, D.; Yan, Y.; Hsu, J.W.P.; Mitzi, D.B. Room-temperature fabrication of a delafossite $CuCrO_2$ hole transport layer for perovskite solar cells. *J. Mater. Chem. A* **2018**, *6*, 469–477. [CrossRef]
24. Monteiro, J.F.H.L.; Monteiro, F.C.; Jurelo, A.R.; Mosca, D.H. Conductivity in (Ag,Mg)-doped delafossite oxide $CuCrO_2$. *Ceram. Int.* **2018**, *44*, 14101–14107. [CrossRef]
25. Shi, J.; Cerqueira, T.F.T.; Cui, W.; Nogueira, F.; Botti, S.; Marques, M.A.L. High-throughput search of ternary chalcogenides for p-type transparent electrodes. *Sci. Rep.* **2017**, *7*, 43179. [CrossRef] [PubMed]
26. Lechermann, F.; Richter, R. Theoretical design of highly correlated electron states in delafossite heterostructures. *Phys. Rev. Res.* **2020**, *2*, 013352. [CrossRef]
27. Lekse, J.W.; Underwood, M.K.; Lewis, J.P.; Matranga, C. Synthesis, Characterization, Electronic Structure, and Photocatalytic Behavior of $CuGaO_2$ and CuGa1–xFexO_2 (x = 0.05, 0.10, 0.15, 0.20) Delafossites. *J. Phys. Chem. C* **2012**, *116*, 1865–1872. [CrossRef]
28. Marquardt, M.A.; Ashmore, N.A.; Cann, D.P. Crystal chemistry and electrical properties of the delafossite structure. *Thin Solid Film.* **2006**, *496*, 146–156. [CrossRef]
29. Nagarajan, R.; Draeseke, A.D.; Sleight, A.W.; Tate, J. p-type conductivity in $CuCr_{1-x}Mg_xO_2$ films and powders. *J. Appl. Phys.* **2001**, *89*, 8022–8025. [CrossRef]
30. Shook, J.; Scolfaro, L.M.; Borges, P.D.; Geerts, W.J. Structural stability and electronic properties of XTO_2 (X = Cu, Ag; T = Al, Cr): An ab initio study including X vacancies and Mg doping. *Solid State Sci.* **2019**, *88*, 48–56. [CrossRef]

31. Kandpal, H.C.; Seshadri, R. First-principles electronic structure of the delafossites ABO_2 (A = Cu, Ag, Au; B = Al, Ga, Sc, In, Y): Evolution of d10–d10 interactions. *Solid State Sci.* **2002**, *4*, 1045–1052. [CrossRef]
32. Durá, O.J.; Boada, R.; Rivera-Calzada, A.; León, C.; Bauer, E.; de la Torre, M.A.L.; Chaboy, J. Transport, electronic, and structural properties of nanocrystalline $CuAlO_2$ delafossites. *Phys. Rev. B* **2011**, *83*, 045202. [CrossRef]
33. Shannon, R.D.; Prewitt, C.T.; Rogers, D.B. Chemistry of noble metal oxides. II. Crystal structures of platinum cobalt dioxide, palladium cobalt dioxide, coppper iron dioxide, and silver iron dioxide. *Inorg. Chem.* **1971**, *10*, 719–723. [CrossRef]
34. Ferri, M.; Elliott, J.; Fabris, S.; Piccinin, S. Establishing best practices to model the electronic structure of $CuFeO_2$ from first principles. *Phys. Rev. B* **2020**, *101*, 155201. [CrossRef]
35. Galakhov, V.R.; Poteryaev, A.I.; Kurmaev, E.Z.; Anisimov, V.I.; Bartkowski, S.; Neumann, M.; Lu, Z.W.; Klein, B.M.; Zhao, T.R. Valence-band spectra and electronic structure of $CuFeO_2$. *Phys. Rev. B* **1997**, *56*, 4584–4591. [CrossRef]
36. Liu, Q.L.; Zhao, Z.Y.; Zhao, R.D.; Yi, J.H. Fundamental properties of delafossite $CuFeO_2$ as photocatalyst for solar energy conversion. *J. Alloy. Compd.* **2020**, *819*, 153032. [CrossRef]
37. Zagorac, D.; Zagorac, J.; Pejić, M.; Matović, B.; Schön, J.C. Band Gap Engineering of Newly Discovered ZnO/ZnS Polytypic Nanomaterials. *Nanomaterials* **2022**, *12*, 1595. [CrossRef]
38. Zagorac, D.; Buyer, C.; Zagorac, J.; Škundrić, T.; Schön, J.C.; Schleid, T. Band-Gap Engineering and Unusual Behavior of Electronic Properties during Anion Substitution of Sulfur in LaFSe. *Cryst. Growth Des.* **2024**, *24*, 1648–1657. [CrossRef]
39. Benko, F.; Koffyberg, F. Preparation and opto-electronic properties of semiconducting $CuCrO_2$. *Mater. Res. Bull.* **1986**, *21*, 753–757. [CrossRef]
40. Tate, J.; Jayaraj, M.; Draeseke, A.; Ulbrich, T.; Sleight, A.; Vanaja, K.; Nagarajan, R.; Wager, J.; Hoffman, R. p-Type oxides for use in transparent diodes. *Thin Solid Film.* **2002**, *411*, 119–124. [CrossRef]
41. Gilbert, T.L. Hohenberg-Kohn theorem for nonlocal external potentials. *Phys. Rev. B* **1975**, *12*, 2111–2120. [CrossRef]
42. Seidl, A.; Görling, A.; Vogl, P.; Majewski, J.A.; Levy, M. Generalized Kohn-Sham schemes and the band-gap problem. *Phys. Rev. B* **1996**, *53*, 3764–3774. [CrossRef] [PubMed]
43. Blöchl, P.E. Projector augmented-wave method. *Phys. Rev. B* **1994**, *50*, 17953–17979. [CrossRef] [PubMed]
44. Perdew, J.P.; Burke, K.; Ernzerhof, M. Generalized Gradient Approximation Made Simple. *Phys. Rev. Lett.* **1996**, *77*, 3865–3868. [CrossRef] [PubMed]
45. Kresse, G.; Hafner, J. Ab initio molecular dynamics for open-shell transition metals. *Phys. Rev. B* **1993**, *48*, 13115–13118. [CrossRef] [PubMed]
46. Kresse, G.; Furthmüller, J. Efficient iterative schemes for ab initio total-energy calculations using a plane-wave basis set. *Phys. Rev. B* **1996**, *54*, 11169–11186. [CrossRef] [PubMed]
47. Kresse, G.; Joubert, D. From ultrasoft pseudopotentials to the projector augmented-wave method. *Phys. Rev. B* **1999**, *59*, 1758–1775. [CrossRef]
48. Heyd, J.; Scuseria, G.E.; Ernzerhof, M. Hybrid functionals based on a screened Coulomb potential. *J. Chem. Phys.* **2003**, *118*, 8207–8215. [CrossRef]
49. Heyd, J.; Scuseria, G.E. Assessment and validation of a screened Coulomb hybrid density functional. *J. Chem. Phys.* **2004**, *120*, 7274–7280. [CrossRef] [PubMed]
50. Krukau, A.V.; Vydrov, O.A.; Izmaylov, A.F.; Scuseria, G.E. Influence of the exchange screening parameter on the performance of screened hybrid functionals. *J. Chem. Phys.* **2006**, *125*, 224106. [CrossRef] [PubMed]
51. Dudarev, S.L.; Botton, G.A.; Savrasov, S.Y.; Humphreys, C.J.; Sutton, A.P. Electron-energy-loss spectra and the structural stability of nickel oxide: An LSDA+U study. *Phys. Rev. B* **1998**, *57*, 1505–1509. [CrossRef]
52. Steiner, S.; Khmelevskyi, S.; Marsmann, M.; Kresse, G. Calculation of the magnetic anisotropy with projected-augmented-wave methodology and the case study of disordered $Fe_{1-x}Co_x$ alloys. *Phys. Rev. B* **2016**, *93*, 224425. [CrossRef]
53. Monkhorst, H.J.; Pack, J.D. Special points for Brillouin-zone integrations. *Phys. Rev. B* **1976**, *13*, 5188–5192. [CrossRef]
54. Köhler, B.U.; Jansen, M. Darstellung und Strukturdaten von Delafossiten $CuMO_2$ (M = Al, Ga, Sc, Y). *Z. Anorg. Allg. Chem.* **1986**, *543*, 73–80. [CrossRef]
55. Shannon, R.D.; Rogers, D.B.; Prewitt, C.T. Chemistry of noble metal oxides. I. Syntheses and properties of ABO_2 delafossite compounds. *Inorg. Chem.* **1971**, *10*, 713–718. [CrossRef]
56. Ishiguro, T.; Ishizawa, N.; Mizutani, N.; Kato, M.; Tanaka, K.; Marumo, F. Charge-density distribution in crystals of $CuAlO_2$ with *d–s* hybridization. *Acta Crystallogr. Sect. B* **1983**, *39*, 564–569. [CrossRef]
57. Shimode, M.; Sasaki, M.; Mukaida, K. Synthesis of the Delafossite-Type $CuInO_2$. *J. Solid State Chem.* **2000**, *151*, 16–20. [CrossRef]
58. Benko, F.; Koffyberg, F. Opto-electronic properties of p- and n-type delafossite, $CuFeO_2$. *J. Phys. Chem. Solids* **1987**, *48*, 431–434. [CrossRef]
59. Shannon, R.D. Revised effective ionic radii and systematic studies of interatomic distances in halides and chalcogenides. *Acta Crystallogr. Sect. A* **1976**, *32*, 751–767. [CrossRef]
60. Ishiguro, T.; Ishizawa, N.; Mizutani, N.; Kato, M. A new delafossite-type compound $CuYO_2$: I. Synthesis and characterization. *J. Solid State Chem.* **1983**, *49*, 232–236. [CrossRef]
61. Crottaz, O.; Kubel, F. Crystal structure of copper(I) chromium(III) oxide, 2H-$CuCrO_2$. *Z. Krist.-Cryst. Mater.* **1996**, *211*, 481. [CrossRef]

62. Chfii, H.; Bouich, A.; Andrio, A.; Torres, J.C.; Soucase, B.M.; Palacios, P.; Lefdil, M.A.; Compañ, V. The Structural and Electrochemical Properties of $CuCoO_2$ Crystalline Nanopowders and Thin Films: Conductivity Experimental Analysis and Insights from Density Functional Theory Calculations. *Nanomaterials* **2023**, *13*, 2312. [CrossRef] [PubMed]
63. Ruttanapun, C.; nguan cheep, M.S.; Kahatta, S.; Buranasiri, P.; Jindajitawat, P. Optical and electronic transport properties of p-type $CuCoO_2$ transparent conductive oxide. In *Proceedings of the ICPS 2013: International Conference on Photonics Solutions*; Buranasiri, P., Sumriddetchkajorn, S., Eds.; International Society for Optics and Photonics; SPIE: Bellingham, WA, USA, 2013; Volume 8883, p. 88831O. [CrossRef]
64. Shi, L.J.; Fang, Z.J.; Li, J. First-principles study of p-type transparent conductive oxides $CuXO_2$ (X = Y, Sc, and Al). *J. Appl. Phys.* **2008**, *104*, 073527. [CrossRef]
65. Duan, N.; Sleight, A.W.; Jayaraj, M.K.; Tate, J. Transparent p-type conducting $CuScO_2$+x films. *Appl. Phys. Lett.* **2000**, *77*, 1325–1326. [CrossRef]
66. Trari, M.; Bouguelia, A.; Bessekhouad, Y. p-Type $CuYO_2$ as hydrogen photocathode. *Sol. Energy Mater. Sol. Cells* **2006**, *90*, 190–202. [CrossRef]
67. Sánchez-Palencia, P.; Hamad, S.; Palacios, P.; Grau-Crespo, R.; Butler, K.T. Spinel nitride solid solutions: Charting properties in the configurational space with explainable machine learning. *Digit. Discov.* **2022**, *1*, 665–678. [CrossRef]
68. Faber, F.; Lindmaa, A.; von Lilienfeld, O.A.; Armiento, R. Crystal structure representations for machine learning models of formation energies. *Int. J. Quantum Chem.* **2015**, *115*, 1094–1101. [CrossRef]
69. Ward, L.; Dunn, A.; Faghaninia, A.; Zimmermann, N.E.R.; Bajaj, S.; Wang, Q.; Montoya, J.H.; Chen, J.; Bystrom, K.; Dylla, M.; et al. Matminer: An open source toolkit for materials data mining. *Comput. Mater. Sci.* **2018**, *152*, 60–69. [CrossRef]
70. Davies, D.W.; Butler, K.T.; Jackson, A.J.; Morris, A.; Frost, J.M.; Skelton, J.M.; Walsh, A. Computational Screening of All Stoichiometric Inorganic Materials. *Chem* **2016**, *1*, 617–627. [CrossRef] [PubMed]
71. Davies, D.W.; Butler, K.T.; Skelton, J.M.; Xie, C.; Oganov, A.R.; Walsh, A. Computer-aided design of metal chalcohalide semiconductors: From chemical composition to crystal structure. *Chem. Sci.* **2018**, *9*, 1022–1030. [CrossRef] [PubMed]
72. Davies, D.W.; Butler, K.T.; Isayev, O.; Walsh, A. Materials discovery by chemical analogy: Role of oxidation states in structure prediction. *Faraday Discuss.* **2018**, *211*, 553–568. [CrossRef]
73. Sammut, C.; Webb, G.I. (Eds.) Leave-One-Out Cross-Validation. In *Encyclopedia of Machine Learning*; Springer: Boston, MA, USA, 2010; pp. 600–601. [CrossRef]